JCI insight

Patient mutations linked to arrhythmogenic cardiomyopathy enhance calpain-mediated desmoplakin degradation

Ronald Ng, Heather R Manring, Nikolaos Papoutsidakis, Taylor Albertelli, Nicole Tsai, Claudia See, Xia Li, Jinkyu Park, Tyler L. Stevens, Prameela J. Bobbili, Muhammad Riaz, Yongming Ren, Christopher E. Stoddard, Paul M.L. Janssen, T. Jared Bunch, Stephen P. Hall, Ying-Chun Lo, Daniel L. Jacoby, Yibing Qyang, Nathan Wright, Maegen A. Ackermann, Stuart G. Campbell

JCI Insight. 2019. https://doi.org/10.1172/jci.insight.128643.

Research In-Press Preview Cardiology Genetics

Arrhythmogenic cardiomyopathy (ACM) is an inherited disorder with variable genetic etiologies. Here we focused on understanding the precise molecular pathology of a single clinical variant in DSP, the gene encoding desmoplakin. We initially identified a novel missense desmoplakin variant (p.R451G) in a patient diagnosed with biventricular ACM. An extensive single-family ACM cohort was assembled, revealing a pattern of coinheritance for R451G desmoplakin and the ACM phenotype. An in vitro model system using patient-derived induced pluripotent stem cell lines showed depressed levels of desmoplakin in the absence of abnormal electrical propagation. Molecular dynamics simulations of desmoplakin R451G revealed no overt structural changes, but a significant loss of intramolecular interactions surrounding a putative calpain target site was observed. Protein degradation assays of recombinant desmoplakin R451G confirmed increased calpain vulnerability. In silico screening identified a subset of 3 additional ACM-linked desmoplakin missense mutations with apparent enhanced calpain susceptibility, predictions that were confirmed experimentally. Like R451G, these mutations are found in families with biventricular ACM. We conclude that augmented calpain-mediated degradation of desmoplakin represents a shared pathological mechanism for select ACM-linked missense variants. This approach for identifying variants with shared molecular pathologies may represent a powerful new strategy for understanding and treating inherited cardiomyopathies.

Patient Mutations Linked to Arrhythmogenic Cardiomyopathy Enhance Calpain-Mediated Desmoplakin Degradation

Ronald Ng[1†], Heather Manring[2,3†], Nikolaos Papoutsidakis[4†], Taylor Albertelli[5], Nicole Tsai[6], Claudia J. See[1], Xia Li[1,4], Jinkyu Park[4], Tyler L. Stevens[2,3], Prameela J. Bobbili[2,3], Muhammad Riaz[4], Yongming Ren[4], Christopher E. Stoddard[7], Paul M.L. Janssen[2], T. Jared Bunch[8], Stephen P. Hall[9], Ying-Chun Lo[10], Daniel L. Jacoby[4]*, Yibing Qyang[4,10,11,12]*, Nathan Wright[5]*, Maegen A. Ackermann[2,3]*, Stuart G. Campbell[1,13]*

[†]Equal Contributions

*Co-corresponding authors

[1] Department of Biomedical Engineering, Yale University, New Haven, CT
[2] Department of Physiology and Cell Biology, Wexner Medical Center, The Ohio State University, Columbus, OH
[3] Dorothy M. Davis Heart and Lung Research Institute, Wexner Medical Center, The Ohio State University, Columbus, OH
[4] Yale Cardiovascular Research Center, Section of Cardiovascular Medicine, Department of Internal Medicine, Yale School of Medicine, New Haven, CT
[5] Department of Chemistry and Biochemistry, James Madison University, Harrisonburg, VA
[6] Department of Molecular, Cellular and Developmental Biology, Yale University, New Haven, CT
[7] Department of Genetics and Genome Science, University of Connecticut Health, Farmington, CT
[8] Department of Cardiology, Intermountain Health, Salt Lake City, UT
[9] Department of Family Medicine, University of Washington School of Medicine
[10] Department of Pathology, Yale School of Medicine, New Haven, CT
[11] Yale Stem Cell Center, Yale University, New Haven, CT
[12] Vascular Biology and Therapeutics Program, Yale School of Medicine, New Haven, CT
[13] Department of Cellular and Molecular Physiology, Yale School of Medicine, New Haven, CT

Conflict of Interest Statement

SGC is founder of and holds equity in Propria LLC. DLJ has received consulting fees from Myokardia, Abbott, and Alnylam. The other authors have declared no conflict of interest exists.

Abstract

Arrhythmogenic cardiomyopathy (ACM) is an inherited disorder with variable genetic etiologies. Here we focused on understanding the precise molecular pathology of a single clinical variant in DSP, the gene encoding desmoplakin. We initially identified a novel missense desmoplakin variant (p.R451G) in a patient diagnosed with biventricular ACM. An extensive single-family ACM cohort was assembled, revealing a pattern of coinheritance for R451G desmoplakin and the ACM phenotype. An in vitro model system using patient-derived induced pluripotent stem cell lines showed depressed levels of desmoplakin in the absence of abnormal electrical propagation. Molecular dynamics simulations of desmoplakin R451G revealed no overt structural changes, but a significant loss of intramolecular interactions surrounding a putative calpain target site was observed. Protein degradation assays of recombinant desmoplakin R451G confirmed increased calpain vulnerability. In silico screening identified a subset of 3 additional ACM-linked desmoplakin missense mutations with apparent enhanced calpain susceptibility, predictions that were confirmed experimentally. Like R451G, these mutations are found in families with biventricular ACM. We conclude that augmented calpain-mediated degradation of desmoplakin represents a shared pathological mechanism for select ACM-linked missense variants. This approach for identifying variants with shared molecular pathologies may represent a powerful new strategy for understanding and treating inherited cardiomyopathies.

Key Words: arrhythmogenic cardiomyopathy, missense mutation, desmoplakin, intercalated disc, calpain

Introduction

Arrhythmogenic Cardiomyopathy (ACM) is an inherited disease characterized by fibro-fatty replacement of the myocardium, ventricular arrhythmias, heart failure and elevated risk of sudden cardiac death (1). Previously known as Arrhythmogenic Right Ventricular Cardiomyopathy, the more inclusive designation of ACM reflects increasing recognition that either ventricle (or both) can be involved (2). The majority of biventricular cases feature primary right ventricular impairment, with secondary left ventricular involvement occurring in the later stages of disease progression (3). However, recent work has identified a subset of cases that present with left ventricular fibrosis, arrhythmias, and a mildly affected right ventricle (4,5).

ACM-linked mutations have been identified in a variety of desmosomal genes, including plakophilin (*PKP)*, junction plakoglobin (*JUP)*, desmoglein (*DSG)*, desmocollin (*DSC)*, and desmoplakin (*DSP)*. Although mutations to desmoplakin comprise only ~5% of ACM cases (1), they have been shown in a large multicenter study to be associated with an unusually high degree of penetrance (6). Truncating mutations to desmoplakin, resulting in lower total protein levels, are linked to more severe outcomes and early occurrences of sudden cardiac death (7,8). Additionally, of the 42 previously reported truncating mutations in desmoplakin, the majority are found in patients with left ventricular disease (7). Therefore, the presence of a truncating desmoplakin variant in an individual indicates significant future risk for developing ACM with left ventricular involvement.

In contrast with truncating mutations, missense mutations to desmoplakin do not appear to have consistent clinical phenotypes. While some literature reports earlier ACM presentation with increased severity as a result of missense mutations (9,10), missense mutations in desmoplakin are not uniformly linked with left ventricular manifestation of ACM (11). The absence of a consistent clinical phenotype for missense desmoplakin variants limits the clinical value of genotyping in the management of ACM and calls for a more nuanced understanding of their molecular pathologies. We have approached the task of elucidating genotype-phenotype relationships for desmoplakin missense variants through a novel combination of

several complementary techniques, including genetic linkage analysis, experimental and computational biophysics, and induced pluripotent stem cell (iPSC)-based disease modeling.

Our efforts initially focused on a specific missense desmoplakin variant (p.R451G) identified in a human cohort. Experimental evidence led to the discovery that the desmoplakin protein encoded by *DSP* R451G showed enhanced calpain vulnerability. Using experimental and in silico tools, we subsequently identified three additional missense desmoplakin mutations that share the molecular phenotype of enhanced calpain-mediated degradation. Significantly, these four mutations together share the clinical phenotype of biventricular ACM. Our data point to a mechanism by which certain desmoplakin missense mutations are functionally equivalent to truncating mutations, leading to the same biventricular ACM phenotype.

In addition to identifying common pathomechanisms between missense desmoplakin variants, the success of this approach supports the potential of in vitro and in silico tools to enhance the value of clinical genetic testing, revealing common disease pathways and paving the way for precision molecular therapies.

Results

The ACM phenotype segregates with a novel mutation in desmoplakin (p.R451G).

The index patient (III-28) was a 44-year-old male who suffered sudden cardiac death during vigorous exercise. The patient had a history of asymptomatic biventricular dysfunction on cardiac MRI (CMR; Figure 1A, MOV S1). Gross examination of the heart during autopsy revealed dilation of the right ventricle and severe fibro-fatty scarring in the left and right ventricles. Hematoxylin and eosin (H&E) and Masson's trichrome staining of myocardial explants from a second individual (III-26) revealed extensive biventricular myocyte disarray and fibro-fatty infiltration (Figure 1B). Following a positive diagnosis for ACM by the 2010 ARVC Task Force criteria, whole exome sequencing identified a novel missense variant in the gene *DSP* (ENST00000379802.8; c.1596CGT>GGT; Chr. 6:7568521, GRCh38.p12) encoding desmoplakin (p.R451G).

We proceeded with cascade genetic screening of 115 additional family members, 45 of whom (39%) were found to carry the desmoplakin R451G mutation [G(+)]. All genetically tested individuals were asked to self-report information about their health status and cardiac symptoms and, in cases where patients were systematically followed by a cardiologist, allow access to their medical records. None of the G(-) patients reported a history of cardiomyopathy or heart failure. We obtained access to records of 21 G(+) individuals, of whom 15 were symptomatic or phenotype positive [G(+)P(+)], by evidence of one or more of the following: a) ventricular dysfunction, dilation or scarring/fat infiltration on imaging studies or autopsy reports in the absence of other causes (e.g coronary ischemia), b) recorded ventricular arrhythmias, c) ICD implant and/or d) sudden cardiac arrest or death (SCD). Of the G(+)P(+) patients, six had evidence of dilated cardiomyopathy, one fulfilled 2010 Task Force criteria for ARVC, and five had biventricular involvement. The three remaining patients experienced ventricular arrhythmias with no evidence of structural heart disease on echocardiography or cardiac MRI. No individual exhibited any connective tissue dysplasias (wooly hair, skin or teeth abnormalities), which can present with some ACM variants (12). The demographic, clinical and imaging data of G(+)P(+) patients in our cohort are presented in Table 1.

Six G(+)P(+) patients (1M, 5F) had sudden cardiac arrest or death at a mean age of 40.6+/-16.2 years; for two of them (M/F, cousins) this was the first manifestation of ACM. Autopsies reported extensive right ventricular fatty infiltration in the first case and severe left ventricular subendocardial fibrosis in the second. Five patients (1M, 4F) have received an implantable cardioverter-defibrillator (ICD, four for primary and one for secondary prevention), with one subsequent appropriate ICD shock. T-wave inversions were observed in electrocardiograms of all G(+)P(+) individuals but no epsilon waves were noted.

In our cohort, there seemed to be no apparent pattern in disease progression. Yearly imaging studies showed stable left ventricular dysfunction for 5 years after diagnosis in one individual (left ventricular ejection fraction = 35%), followed by a gradual decline over the next 4 years (down to 17%). Another individual showed a substantial increase in right ventricular chamber size (right ventricular end-diastolic volume from 134 ml to 252 ml), along with de novo appearance of extensive left ventricular fibrosis (assessed by late gadolinium enhancement) on cardiac MRI, within the span of 12 months (without an obvious precipitator). A third individual followed a moderate gradual decline of left ventricular function (left ventricular ejection fraction from 45% to 28%) over nine years (Figure S1A-D).

Linkage analysis using available clinical data revealed a maximum LOD (logarithm of the odds) score for coinheritance of the ACM phenotype and the p.R451G mutation to be 7.65 ($\theta = 0$). In other words, the odds that the ACM phenotype and p.R451G are not linked are less than one in 10 million. Cardiac palpitations and atrial fibrillation were present in some elderly G(-) individuals, but this was not regarded as evidence of cardiomyopathy for LOD score calculations.

R451G individuals have reduced levels of select proteins at intercalated discs.

To assess the subcellular localization of desmoplakin and other essential intercalated disc proteins we used immunofluorescence. Left ventricular explants obtained during autopsy of individual III-26 reveal a decrease in levels of desmoplakin and connexin-43 at the intercalated disc (Figure 2A). Colocalization

analysis of desmoplakin and N-cadherin (intercalated disc marker) showed a significant reduction (42% loss) in immunoreactive signals of desmoplakin at the intercalated disc compared to a donor control (Figure 2B). Interestingly, connexin-43, an essential gap junction protein, also showed a significant reduction (65% loss) at the intercalated disc (Figure 2B). Altered desmoplakin levels at the intercalated discs have been shown to impair connexin-43 membrane localization (13). Plakoglobin (PKG), another desmosomal protein, was distributed normally with N-cadherin at the intercalated disc.

Engineered Heart Tissues constructed from patient-derived induced pluripotent stem cells exhibit reduced levels of desmoplakin in the absence of conduction velocity defects.

According to previously published reports, decreased amounts of desmoplakin at the intercalated disc may lead to a loss of functional connexin-43 and impaired electrical conduction among neighboring cells (13,14). To test this hypothesis, we created Engineered Heart Tissues (EHTs) grown from induced pluripotent stem cells (iPSCs) of a G(+)P(+) individual and of a healthy G(-)P(-) sibling (Figure S2A-C). In contrast to 2D monolayer culture, 3D EHTs provide a more physiological environment and allow for concurrent biomechanical and electrophysiological characterization of cardiomyocytes. Linear tissue constructs facilitated the concurrent measurement of longitudinal conduction velocity and contractile performance(Figure 3A). Western blots of EHTs showed that R451G EHTs contained significantly lower amounts of desmoplakin compared to wildtype (WT) EHTs (Figure 3C) mimicking patient protein expression patterns (40.0±10.3% decrease, $p < 0.05$). However, there were no overt morphological differences induced by the R451G mutation compared to WT EHTs (Figure 3B). Using a ratiometric fluorescent calcium reporter (Fura-2), calcium transients were measured in EHTs. No significant differences in the calcium handling properties were observed (Figure 3D). Next, we assessed action potential propagation through the EHT. We found no significant change in the conduction velocity between EHTs made with iPSCs expressing R451G mutant or WT desmoplakin (12.21 +/- 1.456 cm/s vs 9.356 +/- 1.525 cm/s SEM, Figure 3E). In order to verify that conduction was happening due to propagation through

gap junctions, we treated our constructs with the gap junction blocker carbenoxolone, and saw a corresponding 37.9% decrease in conduction velocity in both WT and mutant EHTs (Figure S3).

In addition to conduction velocity, we assessed the total and phosphorylated levels of connexin-43 in both WT and mutant EHTs. Notably, mutant EHTs exhibited higher levels of phosphorylated connexin-43 at Ser368 compared to WT EHTs despite a significant reduction in total connexin-43 protein (Figure 3F). Phosphorylation of Ser368 in connexin-43 has been implicated in marking the gap junction for degradation via the ubiquitin proteolytic system which could explain the decrease in overall connexin-43 levels (15).

We next assessed potential changes in mechanical properties of the tissues. Sarcomeres are longitudinally linked to the cell membrane via intermediate filament connections which terminate at desmosomal plaques. Thus, we reasoned that destabilized desmosomes could lead to impaired contractile dynamics. Interestingly, we observed a significant increase in the time to peak contraction in the mutant EHTs compared to WT (0.1853 +/- 0.0034s WT vs 0.2165 +/- 0.0051 s R451G, $p < 0.0001$) without a corresponding difference in peak force (304.8 +/- 41.47μN WT vs 330 +/- 64.53 μN R451G, $p = 0.7110$) or time to 50% relaxation (0.1168 +/- 0.0028s vs 0.123 +/- 0.0036s in WT vs. R451G, $p = 0.2006$, respectively, Figure 3 G-J).

DSP mRNA levels are not reduced in homozygous R451G EHTs

After recapitulating reduced desmoplakin levels in patient EHTs, we then investigated whether the protein loss was a result of lowered levels of mRNA transcript. In order to eliminate possible confounding secondary genetic factors, we utilized CRISPR/Cas9 to produce a novel cell line homozygous for DSP R451G (R451G/R451G), derived from a commercially available healthy control line (WT/WT, Figure 4A). RT-qPCR was performed on 14-day-old EHTs made with either R451G/R451G or isogenic WT/WT cardiomyocytes to probe for any differences in *DSP* transcripts. Primers targeted regions upstream of the R451G mutation, flanking the mutation, and downstream of the mutation. Expression levels of *DSP* mRNA were not significantly different between the two cell lines at any of the targeted regions (Figure 4B). This suggests that the mutation does not result in altered processing of *DSP* mRNA.

The R451G mutation does not overtly affect the structure or stability of desmoplakin.

With immunofluorescence analysis of a patient sample and EHT evidence indicating a loss of desmoplakin protein in the absence of depressed mRNA levels, we hypothesized that the R451G variant destabilizes the protein and allows increased degradation. In order to test this hypothesis, we turned to in silico modeling and biophysical structural analysis of the WT and mutant protein. Desmoplakin is a modular protein with three distinct regions (Figure 5A) (16). The NH_2-terminal third of the protein is composed of six α-helical spectrin repeats (SR) and a Src homology (SH) 3 domain. The middle portion of desmoplakin consists of a coiled-coil rod domain necessary for homodimerization and the COOH-terminus contains three plakin repeat domains. The R451G variant maps to the SH3 domain, which is a known hot-spot of ACM-associated mutations. 24% of pathological desmoplakin variants map to a region spanning ~200 amino acids within the NH_2-terminus of the protein (4,17,18,19,20). However, circular dichroism experiments did not reveal any significant differences in either helical content or global protein stability between the WT and R451G constructs (Figure 5C). In addition, molecular dynamic (MD) simulations show no gross structural deviations between the WT and mutant protein (Figure 5B). A recent report by Daday *et al* found the SH3 domain to remain correctly folded despite applied forces large enough to destabilize other domains in desmoplakin (21). It is therefore not entirely surprising that desmoplakin remains macroscopically unchanged despite a single residue substitution (21). We conclude that global protein structure stability is unaffected by the introduction of a glycine at position 451 of desmoplakin.

R451G desmoplakin is more sensitive to calpain-mediated degradation

We next investigated more regulated means of protein destabilization that could lead to loss of desmoplakin protein at the intercalated disc. It has previously been shown that a missense mutation in plakophilin-2 leads to increased degradation by calpain, a calcium-dependent protease (22). We tested the hypothesis that desmoplakin is also a target for calpain-mediated degradation. Healthy human donor heart lysates exposed

to exogenous calpain showed a complete loss of full-length endogenous desmoplakin compared to lysates with no treatment (Figure 6B). In addition, simply increasing the exogenous calcium levels significantly reduced full-length desmoplakin levels, presumably by activation of endogenously expressed calpain present in the myocardial lysate(Figure 6B). These data suggest that desmoplakin is indeed a target for calpain-mediated degradation.

To assess where calpain may target desmoplakin, we performed in silico analysis using publicly available prediction algorithms (GSP-CCD 1.0 and calpcleave (23,24)). These algorithms predicted 14 calpain target sites within the NH_2-terminus of desmoplakin. We further limited our search to sites that were (a) expected to be targeted with both prediction algorithms, (b) within 7 Å of the mutation 'hot-spot' area, and (c) solvent exposed. With these criteria, only two sites remained, at positions 449 and 455. Although these sites are quite near each other in sequence and reside in the same loop, we focused our attention on the 449 site due to it being a better fit for calpain targeting and the more solvent-exposed of the two sites (Figure 6A). Within 7 Å of this site, there exist 11 intra-residue hydrogen bonds or electrostatic interactions, based on the x-ray structure (25) (Figure 6A). These noncovalent interactions comprise a 3-loop region, which functions to hold the putative calpain target site close to the SH3 domain and a loop of a neighboring spectrin repeat. In an MD simulation of 100 ns, WT desmoplakin maintains, on average, 9.18 of these noncovalent bonds. In contrast, simulations on the R451G variant have only 5.83 bonds (Figure 6C). In addition, there is a wider distribution of bonds present in R451G, which may suggest increased flexibility. Thus, the putative calpain target site is not as tightly tethered to the rest of the molecule in the R451G mutant. This finding is recapitulated in examination of exposed surface area for residues 447-451; the introduction of the glycine at position 451 significantly increased the exposed surface area of that region compared to WT (Figure 6D-E). These simulations suggest that the R451G mutation causes the putative 449 calpain target site to be hyper-available for protease activity.

To test the MD prediction that the R451G mutation increases susceptibility of desmoplakin to calpain, we performed calpain assays using recombinant desmoplakin (aa 1-883) WT and mutant proteins. WT

desmoplakin was stable even in the presence of calpain and 10mM calcium (Figure 7A). In comparison, the R451G protein showed increased degradation after 10 minutes and significant loss of protein after 30-minute exposure to calpain and calcium (Figure 7B-C). Mutant desmoplakin exhibited markedly faster degradation compared to WT. 40% of the R451G desmoplakin was lost in the first 30 minutes compared to minimal loss of the WT protein. These results, in conjunction with the MD data, support our hypothesis that the main molecular consequence of the R451G mutation is to increase calpain target site exposure and subsequently promote desmoplakin degradation.

EHTs expressing mutant desmoplakin respond differently to calpain inhibition

We next sought to demonstrate directly that lower desmoplakin abundance in EHTs expressing desmoplakin R451G is due to enhanced calpain-mediated degradation. Desmoplakin protein abundance was measured in EHTs made from R451G/R451G or control cells, with and without 72-hour treatment with the calpain inhibitor MDL-28170. Analysis of desmoplakin protein levels with two-way ANOVA revealed a significant interaction between expression of desmoplakin R451G and the presence of calpain inhibitor, meaning that the effect of MDL-28170 on desmoplakin protein levels depended on genotype (Figure 8A-B). Specifically, MDL-28170 had the effect of decreasing desmoplakin in control EHTs, while levels were unchanged in EHTs expressing only desmoplakin R451G. Thus, calpain inhibition raised desmoplakin protein levels in R451G/R451G EHTs relative to control. These results are supportive of a mechanism whereby *DSP* R451G affects protein stability, resulting in diminished abundance of the desmoplakin in spite of normal transcript levels.

Pathogenic ACM–linked mutants are predicted to have varying degrees of calpain susceptibility.

The R451G mutation occurs in a reported “hot-spot” region of desmoplakin for ACM-linked variants (residues 280-515) (Figure 9A). To see if this was the primary patho-mechanism of other mutations in

desmoplakin, we conducted similar predictive MD simulations on S299R, N375I, S442F, I445V, N458Y, K470E, and S507F. Simulations on four of the variants (N375I, I445V, N458Y, and K470E) mimic WT in both the number of interactions and surface area exposure (Figure 9B-C, Table 2). However, MD simulations of three other variants (S299R, S442F, S507F) show both a reduced number of intermolecular interactions and an increase in the exposed surface area of the putative calpain target site (Figure 9B-C, Table 2). This led us to predict that S299R, S442F and S507F would have increased susceptibility to calpain degradation.

Using a recombinant calpain assay, the three variants S299R, S442F, and S507F were found to degrade more rapidly and completely compared with the other mutants. Degradation rates for N375I, I445V, N458Y, and K470E variants were not significantly different from WT (Figure 9D). Thus, our results suggest that a subset of ACM-associated missense mutations within this hot-spot region of desmoplakin act primarily through destabilizing molecular interactions that protect calpain target sites. The significant correlation ($p<0.05$) between MD simulation parameters (exposed surface area of the calpain target site and number of intramolecular interactions) and in vitro biochemical properties (total protein remaining following calpain degradation and rate of degradation) validates the in silico predictions of calpain vulnerability (Figure 9E).

Discussion

Truncating desmoplakin mutations have been linked to a biventricular or predominantly left ventricular presentation of ACM, while missense desmoplakin mutations have proven unpredictable in terms of the affected chamber. Here, we present evidence for the first time that some desmoplakin missense variants mimic truncating alleles by introducing pathological vulnerability to calpain proteolysis and subsequent desmoplakin insufficiency. Furthermore, the subset of four calpain-vulnerable missense mutations we have identified share a biventricular ACM phenotype reminiscent of that seen for truncating mutations. In addition to revealing a novel mechanism for desmoplakin variant pathogenicity, our study supports the idea that detailed biophysical understanding of mutational consequences can clarify genotype-phenotype relationships in ACM.

Care was taken in this study to align clinical, cellular, molecular, and genetic information in an unbroken chain of evidence to establish the pathogenicity of *DSP* R451G and its associated mechanism. A large ACM family provided conclusive data on the clinical phenotype and penetrance of this mutation. The observed deficiency of desmoplakin at the intercalated discs of patient tissue was recapitulated in myocardial tissue engineered from the iPSC line of an affected patient. A genetically engineered cell line homozygous for desmoplakin R451G confirmed dramatic desmoplakin loss in spite of normal levels of *DSP* transcript. Molecular dynamic predictions of enhanced calpain target site exposure in R451G desmoplakin were supported by significantly accelerated degradation with in vitro experiments. Calpain inhibition in EHTs expressing exclusively desmoplakin R451G showed a partial restoration of desmoplakin levels relative to control. These results document clear risk for patients carrying *DSP* R451G and suggest possible avenues for therapeutic intervention.

Additional questions about cell- and organ-level disease mechanisms in ACM remain, but our work does provide new insights in this vein. The early phenotypes evident in patient-derived EHTs were somewhat surprising. While these EHTs recapitulated the loss of desmoplakin and connexin 43, we did not see the expected change in electrical propagation. Numerical simulations have shown that a 50% loss in gap

junction conductance leads to only modest changes in conduction velocity (26), hence the observed decrease in connexin-43 may not be sufficient to induce impaired conduction. This in line with another study, which reported arrhythmogenic potential in an ACM model system in spite of normal conduction velocity (27). EHTs expressing mutant desmoplakin exhibited slower force development compared to EHTs expressing WT desmoplakin. This is in agreement with evidence that localized regions of dyskinesia represent an early disease marker (28).

In addition to R451G, we investigated several other known pathogenic missense desmoplakin mutations (S299R, N375I, S422F, I445V, N458Y, K470E, and S507F) to see if they presented with a similar patho-mechanism and resultant phenotype. Although three seemed to function similarly to R451G, two of the other variants (N458Y and K470E) were predicted not to cause any change to the putative calpain site (447-451). Work by others has shown that in fact the N458Y mutation alters desmoplakin function in an alternate way (possibly by weakening EB-1 binding interactions) (13). In that study, human keratinocytes expressing these variants showed no decrease in the amount of expressed desmoplakin compared to WT controls. It appears as though variants even within close proximity can give rise to distinct molecular and clinical pathologies (29).

Perturbations to normal calpain-mediated degradation may be a common ACM mechanism, not limited to mutations in desmoplakin. Kirchner *et al*. presented evidence that a missense mutation in plakophilin-2 leads to increased degradation through calpain (22). Although this mutation appeared in a patient who met the 2010 ARVC task force criteria, linkage of the mutation to the ARVC phenotype was called into question by some due to the small size of the family in that study (22). Our work lends support to the conclusions of Kirchner *et al*. by demonstrating a similar mechanism in a very large kindred of sufficient size to provide unambiguous statistical linkage. Together, the two studies point to increased calpain-mediated proteolytic degradation as a primary disease mechanism for a subset of ACM patients and suggest that calpain should be targeted in research for novel therapies.

Other findings presented here further highlight the need for treatment strategies that match the diverse underlying molecular pathologies associated with ACM. Immunofluorescence imaging of cardiac tissue from an R451G patient autopsy showed no decrease in plakoglobin levels at the intercalated discs, even in a late stage with severe myocyte disarray, adipogenesis and fibrosis (Figure 1-2). This conflicts with previous reports that loss of plakoglobin from the intercalated disc is a universal feature of ACM-linked desmosomal mutations (30). Our observations, together with similar findings in a mouse model of ACM (31) suggest that nuclear localization of plakoglobin and consequential aberrant Wnt/β-catenin signaling is not a necessary condition for biventricular ACM presentation. Rather, that mechanism may dominate in an alternate subset of ACM mutations. This seems to be the case in work by Asimaki *et al*., who found that SB216763, an inhibitor of GSK3β and thus activator of the canonical Wnt pathway, was able to correct protein mislocalization in a zebrafish model expressing mutant plakoglobin (JUP 2057del2) (32). SB216763 has also shown efficacy in models expressing selected ACM-associated mutations to PKP2 or DSG2 (33). Importantly, each of these mutations were demonstrated to trigger plakoglobin mislocalization, suggesting overall that GSK3β inhibition therapy may be uniquely suited to mutations having this shared phenotype (33). This heterogeneity of molecular pathologies, including the possible susceptibility to degradation by calpain that we have uncovered, should be taken into account when exploring and testing treatment strategies for ACM.

Whole exome sequencing of cardiomyopathy patients commonly reveals variants of unknown significance (34). A persistent clinical challenge is to differentiate between a true disease-causing mutation and one of many harmless variants. Recent work showed that 16% of healthy individuals harbor a single nucleotide polymorphism in one of the desmosomal genes (35). Current computational tools based on heuristic interpretation, such as SIFT or PolyPhen2 often mischaracterize the pathogenicity of unknown variants. For example, a meta-analysis showed that out of 209 pathogenic variants clearly linked to clinical ACM, Poly-Phen2 classified 41 of them as benign (36). While genetic linkage analysis is an effective way to classify variants by pathogenicity, it is not always feasible due to the difficulty of assembling a large kindred

necessary for sufficient statistical power. Our approach, using bilateral in silico and in vitro modeling aimed at elucidating primary molecular patho-mechanisms may ultimately address limitations posed by existing methods, resulting in more accurate predictions of pathogenicity for variants of unknown significance.

Foremost among the questions raised by this work is the need to identify a means of blocking calpain-mediated desmoplakin degradation with greater specificity. A calpain inhibitor such as MDL-28170 appears to have wide-spread effects on cardiomyocyte function such that it actually decreases desmoplakin in control cells. In desmoplakin R451G EHTs, it appears that non-specific desmoplakin loss (as observed in control cells) was balanced by increased desmoplakin levels from lowered calpain mediated degradation. Hence, MDL-28170 treatment resulted in only a modest relative restoration of desmoplakin levels in EHTs expressing desmoplakin R451G rather than an absolute increase. It is clear that future therapeutic strategies must interfere with calpain-desmoplakin interactions with high specificity.

The nuclear localization, if any, of desmoplakin cleavage products promoted by R451G was not considered in this study. Literature has shown that cleavage products of mutant junctophilin-2 can translocate to the nucleus, where they impact transcription (37). Our measurements of protein levels and localization did not show evidence of cleavage products translocating to the nucleus, but it is possible that some degradation products were not recognized by the antibodies used.

Another area of future work lies in developing clearer connections between clinical disease and in vitro phenotypes in iPSC-derived EHTs. Desmoplakin R451G EHTs did not exhibit any arrhythmogenic markers such as decreased conduction velocity or other pathological features such as lipid droplet deposition or increased apoptosis. Other studies using human iPSCs to model ACM have failed to observe decreases in conduction velocity, and only observed differences in action potential shape and presence of lipid droplet after concerted attempts to induce metabolic maturation (27,38,39). It therefore seems that improved metabolic maturation will be a prerequisite to observing clear functional effects of desmoplakin loss in our EHT system.

In summary, we have presented evidence that specific missense desmoplakin variants cause ACM characterized by prominent LV involvement, fibrosis, and sudden death. Further, we have presented evidence that the primary effect of *DSP* R451G is increased susceptibility to proteolytic degradation by calpain leading to desmoplakin insufficiency. The use of in silico simulation tools to quantify aberrant molecular behavior triggered by this mutation made it possible to identify other mutations linked to ACM that function through the same mechanism.

Materials and Methods

Clinical Analysis and Genetic Linkage

Whole exome sequencing was conducted on proband samples (III-28). Following identification of the R451G mutation in desmoplakin, additional participating individuals submitted saliva samples, which underwent targeted sequencing focused at identifying the R451G variant in desmoplakin. A sample of patient genomic DNA was used to amplify exon 11 of the *DSP* gene by Polymerase chain reaction (PCR) using the following conditions: Denaturation at 96°C for 2 minutes followed by 35 cycles of 30 seconds at 96°C, 30 seconds at 55°C, and 40 seconds at 72°C. Sanger Sequencing was carried out on the products of this reaction on an Applied Biosystems 3730xL DNA Analyzer using Applied Biosystems Big Dye chemistries. All protocols and consent forms were prepared in accordance with and approved by the Yale University Institutional Review Board. ACM phenotypes were explored through medical record, history and autopsy data reviews. Linkage analysis was conducted using LINKAGE (40). The frequency for alleles 1 and 2 were 0.804 and 0.196 as informed by the occurrence rate in the pedigree. A conservative disease penetrance of 0.5 was used, but our data suggests that the actual penetrance may be closer to 0.9 (14/15 mutation carriers older than 60 years of age expressed at least one ACM phenotype).

Procurement of Human Heart Samples

The studies on human heart tissue were performed under the guidelines of the Declaration of Helsinki, with oversight by the Institutional Review Boards at Yale University and The Ohio State University (protocol numbers HIC1005006865 and 2012H0197, respectively). Heart sample harboring the desmoplakin R451G variant was obtained from patients III-26 and III-28 during autopsy. Non-failing donor heart samples were obtained in collaboration with the Lifeline of Ohio Organ Procurement program from an organ donor without diagnosed heart failure whose heart was not suitable for transplantation. The donor heart was removed and immediately submersed in ice-cold cardioplegic solution containing 110 mM NaCl, 16 mM

KCl, 16 mM $MgCl_2$, 10 mM $NaHCO_3$, and 0.5 mM $CaCl_2$. Tissues were either snap frozen or prepared for histological analysis, below. Biopsies from the free wall of the left and right ventricles were used in this study.

Histology and Immunofluorescence

Following fixation in formalin and paraffin embedding, thin sections from individual III-28 were stained with hematoxylin and eosin and with Masson's trichrome. Histology analysis was performed using Olympus BX40 light microscope with tilting binocular head. Photomicrographs were taken using Diagnostic Instruments SPOT RT-SE™ Digital Camera system.

Immunofluorescence was performed on paraffin-embedded non-failing donor hearts and biopsies from individual III-26 using standard protocols (41,42). Prepared sections were imaged at a magnification of 40x with a Zeiss 780 confocal fluorescent microscope. Colocalization analysis was completed using a custom MATLAB script following the Mander's Correlation Coefficient method (43).

In Silico Calpain Prediction

Calpain target sites were predicted using GPS-CCD and calpcleave (23,44). The 449 site was deemed the most likely cut site due to the likelihood of calpain to cleave, the proximity to the mutation hot-spot, and solvent accessibility.

Computational Modeling of Wildtype and Mutant Desmoplakin

Computational modeling was done using the human wildtype desmoplakin Protein Data Bank (PDB) number 3R6N (25). The desmoplakin S299R, N375I, S442F, I445V, R451G, N458Y, K470E, and S507F

mutation models were generated with the 'swap residue' command in the computer program YASARA and allowed to equilibrate for at least 60 ns in explicit solvent at 310K, 150 mM NaCl, as previously described (45,46). All hydrogen bonds and electrostatic interactions within 7 Å of the putative calpain target site in the original structure were surveyed every 25 ns, and the data were tabulated using YASARA. Cutoff distances for H-bonds was set to 3.5 Å and electrostatic interactions to 5 Å. A snapshot of each mutant was generated every 10 ns in YASARA, and the exposed surface area of residues 447-451 was calculated for each time point using Pymol (23). Calculations and statistics were performed in R v3.4.0, and data were plotted using ggplot2 (24).

Site-directed Mutagenesis and Recombinant Protein Production

The NH_2-terminus of human desmoplakin (aa 1-883; Addgene plasmid #32227) was directionally cloned into the pGex-4T1 vector, primers listed in Table S1 (47). The S299R, N375I, S442F, I445V, R451G, N458Y, K470E, and S507F mutations were individually introduced into the wildtype desmoplakin$_{1\text{-}883}$ using the QuikChange Site-directed mutagenesis Kit (Agilent Technologies, Santa Clara, CA) according to the manufacturer's instructions. Introduction of each mutation was confirmed via sequencing. Wildtype and mutant desmoplakin$_{1\text{-}883}$ proteins were produced in bacteria as GST-fusion proteins using the pGEX-4T1 vector system according to established methods (42).

Circular Dichroism (CD)

CD was obtained using a 3 mm quartz cuvette on a JASCO J-810 spectrapolarimeter in 5 ^{o}C increments from 25-90°C. Experiments were completed in triplicate, using 1-3 μM protein in PBS, pH 8.0. CD spectra were taken from 300-200 nm.

Calpain Assays

Two types of calpain assays were performed; Type 1: using human heart lysates and Type 2: using recombinant affinity purified protein (48–51). For Type 1, donor human heart tissue was homogenized with a 10 mM Tris HCl-0.32 M sucrose buffer followed by centrifugation. Lysates were diluted to 6 mg/mL with homogenization buffer and an equal volume of assay buffer (40 mM Tris HCl, 50 mM NaCl, 2 mM DTT) with and without 10 mM $CaCl_2$ and with and without calpain (Sigma C6108). Reactions were incubated at 37°C for 30 minutes, quenched, and analyzed by SDS-PAGE and western blot.

For Type 2, 25 μg of purified recombinant protein was diluted in assay buffer, with 10 mM $CaCl_2$ and calpain. Reactions were incubated at 37°C for 30 minutes; 5 μg of protein were removed at each time point, quenched, and analyzed by SDS-PAGE followed by staining with Sypro Ruby total protein stain according to the manufacturer's instructions. Quantification of the total amount of protein remaining and the rate of degradation was calculated via densitometry obtained from ImageJ software (NIH). The rate of protein degradation was determined via the slope of the best-fit linear line. Values for at least three independent replicates were averaged for each desmoplakin$_{1\text{-}883}$ protein.

Induced Pluripotent Stem Cells and Engineered Heart Tissues

Human induced pluripotent stem cell lines were generated from a family member with the R451G mutation and no clinically diagnosable phenotype (III-35); and an unaffected family member with no mutation in desmoplakin (III-36). Blood was collected in accordance with the Yale and Stanford Institutional Review board. Peripheral blood mononuclear cells (PBMCs) were isolated and then reprogrammed to iPSCs via the Sedai virus (CytoTune®-iPS 2.0 Sendai Reprogramming Kits, Invitrogen) in Joseph C. Wu group, Stanford Cardiovascular Institute. IPSCs were maintained on mouse embryonic fibroblast layers in human embryonic stem cell medium (20% Knock out Serum Replacement, 1% Glucose, 1% NEAA, 55uM β-mercaptoethanol in DMEM/F12 basal medium containing bFGF 10 ng/ml) at 5% CO_2 and 37°C. Cells were

stained for pluripotency markers OCT4, SSEA-4, NANOG, TRA-1-60, and alkaline phosphatase (Fig S2A). Karyotyping demonstrated stable chromosomal integrity in iPSC lines (Fig S2B). An additional healthy control cell line was purchased from Coriell Institute for Medical Research (GM23338). Genetic modification was conducted on GM23338 hiPSCs to generate a homozygous R451G desmoplakin mutant line. Detailed methods available in the online supplement.

Prior to differentiation iPSCs were cultured on Matrigel-coated plates (BD Biosciences). Cells were maintained in mTeSR-1 media (StemCell Technologies) until they reached confluency. Once confluent, cells underwent cardiac differentiation as described (52). Briefly, cells were cultured in RPMI with B27 minus insulin and 20μM CHIR99021 (Selleck Chemicals). After 24 hours, the media was replaced with fresh RPMI with B27 minus insulin. Forty-eight hours after this change, half the media was replaced with RPMI with B27 minus insulin and 5 μM Wnt Inhibitor IWP4 (Stemgent). From day 9 onwards, the cells were incubated with RPMI with B27. Media was replaced every other day with fresh media. Only wells with beating clusters visible by day 10 were used for experiments.

Engineered Heart Tissues (EHTs) were constructed via previously published methods outlined in Schwan *et al* 2016 (52). In brief: porcine hearts were dissected and blocks of the left ventricular free wall were removed. Blocks were cryo-sectioned into slices parallel to the fiber direction to a thickness of 150μm. The slices were incubated in a lysis buffer (10 mM Tris, 0.1% w/v EDTA, pH 7.4) for 2 hours before being attached to PTFE clips. Tissues were incubated in sodium dodecyl sulfate (0.5% w/v in PBS) for 40 minutes with gentle agitation. Tissues were washed 3 times in PBS before being incubated in DMEM + 10% FBS with 1x Penicillin-Streptomycin overnight. Cardiomyocytes were dissociated via incubation with Accutase and seeded onto the scaffold at a density of 1.67 million cells per scaffold. EHTs were cultured for 2 weeks under electrical stimulation using a custom-built bioreactor before mechanical characterization was conducted.

Mechanical testing was performed on a custom-built setup using a force transducer (WPI KG-7) and length control via micro manipulators (Siskiyou). Tissues were tested in Tyrode's solution (140 mM NaCl, 5.4

mM KCl, 1 mM $MgCl_2$, 25 mM HEPES, 10 mM glucose, and 1.8 mM CaCl; pH adjusted to 7.3.) Calcium transients were measured using the ratiometric dye Fura-2 (Millipore). Loading of the dye was achieved using Tyrode's solution with 17 µg/ml Fura-2 AM, 0.2% Pluronic F127, and 0.5% Cremophor EL. Tissues were incubated with the Fura-2 solution for 20 minutes at room temperature and then washed with fresh Tyrode's for 10 minutes at 37° C. The selected region was excited with a rapidly alternating sequence of 340/380 light and the response centered at 510 nm was collected by a photomultiplier tube. Custom MATLAB post processing routines separated the interleaved excitation response signals and computed a final ratiometric response. Conduction velocity was measured by tracking the calcium activation time, as the tissue was locally stimulated using a small bipolar electrode. As this point stimulus was moved further from the measurement region, the measured calcium upstroke was progressively delayed in time. Conduction velocity was determined as the slope of line between distance moved and upstroke delay. Contraction force characteristics, including time from stimulus to peak force, time from peak force to 50% relaxation, and magnitude of peak force were extracted from force transducer recordings.

Individual snap-frozen EHT were homogenized in 10 mM sodium phosphate buffer pH 6.8, 2 mM EDTA, 10 mM NaN_3, 120 mM NaCl, 2% SDS, 1% β-mercaptoethanol lysis buffer with protease inhibitor. Lysates were analyzed via SDS-PAGE and western blot. Total desmoplakin protein was normalized to the loading control (sarcomeric actin) and calculated as a fold-change compared to the wildtype EHT.

For RT-qPCR experiments, snap-frozen EHTs were homogenized in Trizol in order to isolate total RNA and cDNA was synthesized using the iSCript cDNA synthesis kit (Bio-Rad, USA). 10ng of cDNA was used for quantitative PCR using SYBR green mix (Bio-Rad, USA) in a total reaction volume of 15µL. PCR was conducted on the C1000 Cfx96 Touch Real-Time PCR. Expression levels were calculated according to the ΔCT method normalized to cTnt mRNA levels. Complete primers can be found in the Supplemental Methods.

Calpain inhibition experiments were conducted via incubation of tissues for 72 hours in 25μM MDL-28170 (Sigma) dissolved in DMSO. After incubation, EHTs were collected and homogenized for desmoplakin protein analysis.

Antibodies

Antibodies used include N-cadherin (1:500; Pierce 33-3900), desmoplakin (1:400 (immunofluorescence), Abcam ab14418; 1:2000 (western blotting), Abcam ab71690 & ab109445), plakoglobin (1:500; Abcam ab15153), connexin-43 (1:500; Abcam ab11370), GAPDH (1:5000; Sigma G8795), sarcomeric actin (1:2000; Sigma Aldrich A2066), and phospho-connexin-43 Ser368 (Millipore AB3841; 1:2000).

Statistical Analyses

Reported whole-cell data is represented by the mean and standard error of the mean. Groups of 2 were compared with the unpaired student's t-test with a Bonferroni post-hoc correction applied where noted. Multiple comparisons were done with one or two-way analysis of variance (ANOVA). P-values of < 0.05 were considered significant.

Study Approval

All protocols and consent forms were prepared in accordance with and approved by the Yale University Institutional Review Board. The studies on human heart tissue were performed under the guidelines of the Declaration of Helsinki, with oversight by the Institutional Review Boards at Yale University and The Ohio State University (protocol numbers HIC1005006865 and 2012H0197, respectively).

Author Contributions

RN, HM, NP, DLJ, YQ, NW, MAA, and SGC designed the research studies. RN, HM, TA, XL, JP, TLS, PJB, MR, and YR conducted experiments. NT, CS, NP, YCL, SPH, TJB, and DLJ collected and analyzed clinical data. RN, HM, TA, MR, YQ, NW, MAA, and SGC performed analysis of experimental data. PMLJ provided research materials. RN, HM, NP, DLJ, YQ, NW, MAA, and SGC wrote and edited the manuscript.

Acknowledgements

This work was funded by the National Institute of Health (1R01HL131940 to YQ, HL116778 to MAA), National Science Foundation (REU CHE-1757874 and RUI MCB-1607024 to NTW), the Department of Defense (11959515 to YQ), and the American Heart Association (17GRNT33410446 to SGC). We would also like to acknowledge funding provided by Saving Tiny Hearts Society (to MAA) and a private research gift (to SGC).

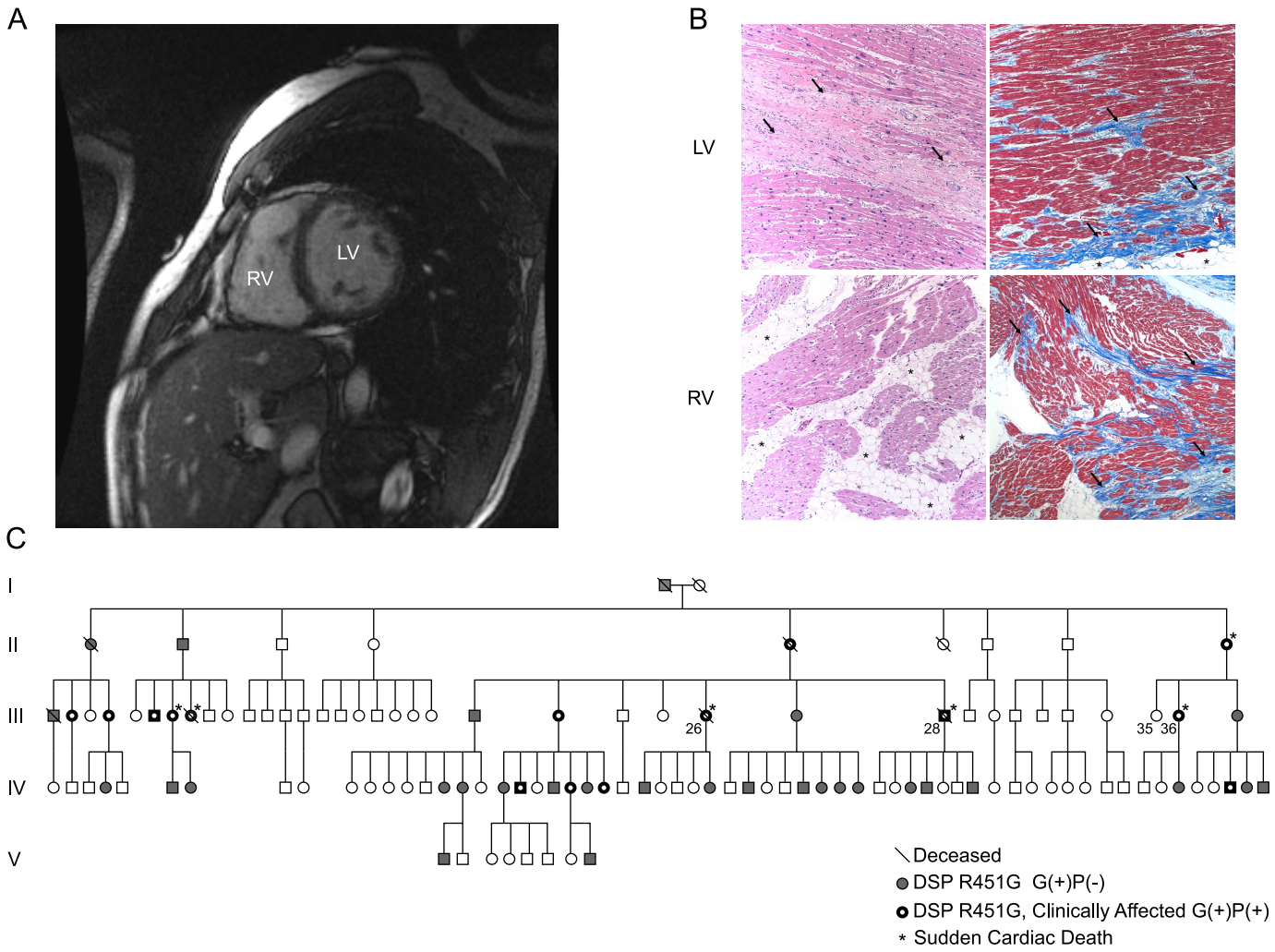

Figure 1: Patient presenting with genetically linked ACM (A) Short-axis cardiac magnetic resonance image of the proband (III-28) one decade prior to a sudden cardiac death episode. Dilation of the left ventricle (LV) and right ventricle (RV), and RV wall thinning are clearly evident. **(B)** Representative images of cardiac biopsy from a second sudden death victim, individual III-26, showing hallmarks of arrhythmogenic cardiomyopathy (ACM) including extensive biventricular myocyte disarray and fibro-fatty infiltration. Images are hematoxylin and eosin (H&E) stained sections (left) and Masson's Trichrome stained sections (right) from the LV (top pair) and RV (bottom pair). All images were obtained at 100x magnification. Histology of the RV free wall shows an extensive fatty infiltrate (arrows) and areas of full-thickness replacement of RV myocardium by adipose tissue. The residual muscle is present in a bandlike or wave-front pattern (H&E). Trichrome staining highlights transmural fibrofatty infiltration by the fibrotic tissue in blue (arrows). Histology of the LV shows patchy fibrosis (arrows, H&E). Trichrome staining highlights patchy fibrosis (arrows) and mild subepicardial adipose tissue replacement (stars). **(C)** Extended pedigree of proband. Open symbols represent unaffected individuals that also lack the DSP R451G mutation. Shaded symbols represent individuals that carry the R451G mutation but do not yet show clinical phenotype (G(+)P(-)). Black symbols with a white center represent mutation positive individuals with clinical symptoms of ACM (G(+)P(+)). Slashes denote deceased individuals. Asterisks denote individuals who experienced a sudden cardiac death event. Analysis revealed a highly significant linkage between DSP R451G and the ACM phenotype (LOD score 7.65).

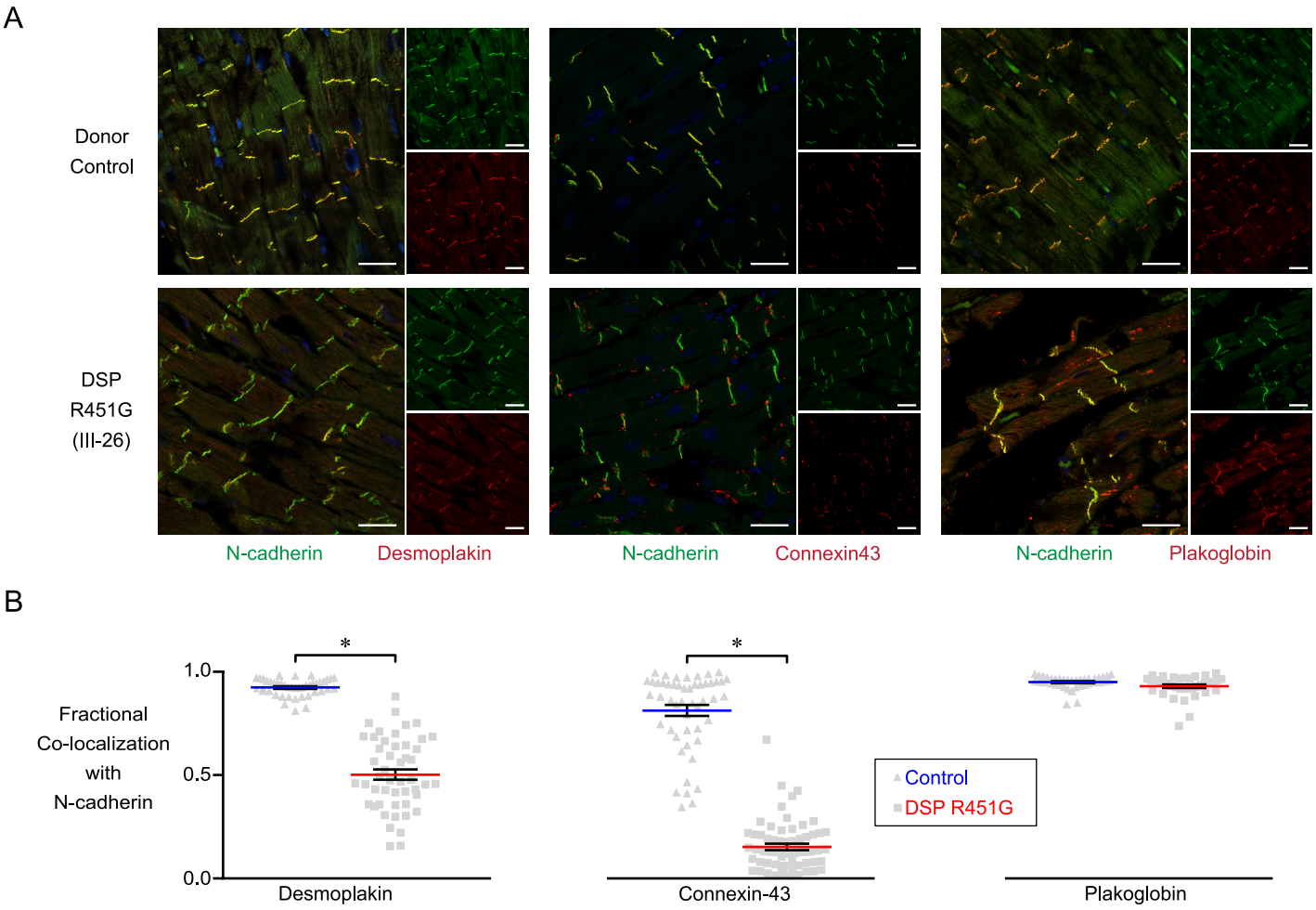

Figure 2: Significant loss of desmoplakin and connexin-43 at the intercalated discs in an R451G-positive patient with clinical ACM diagnosis. (A) Representative immunofluorescence images from a donor control (OSU 652849) and patient III-26, who carried DSP R451G and was clinically diagnosed with ACM. Left ventricular tissue was stained with antibodies for desmoplakin (left), connexin-43 (middle) or plakoglobin (right). Tissues were co-stained with an antibody for N-cadherin (green), identifying intercalated discs. Scale bars represent 40 micrometers. **(B)** Manders colocalization analysis of selected protein overlap with N-cadherin at intercalated disks. Individual III-26 had significantly lower amounts of desmoplakin (n = 42 control and n = 49 patient) and connexin-43 (n =50 control and n = 60 patient) at intercalated discs as compared with donor controls. There was no significant loss of plakoglobin at the intercalated disk (n = 40 control and n = 37 patient). *P < 0.0001 using 2-tailed unpaired t test with Bonferroni correction. Error bars represent SEM.

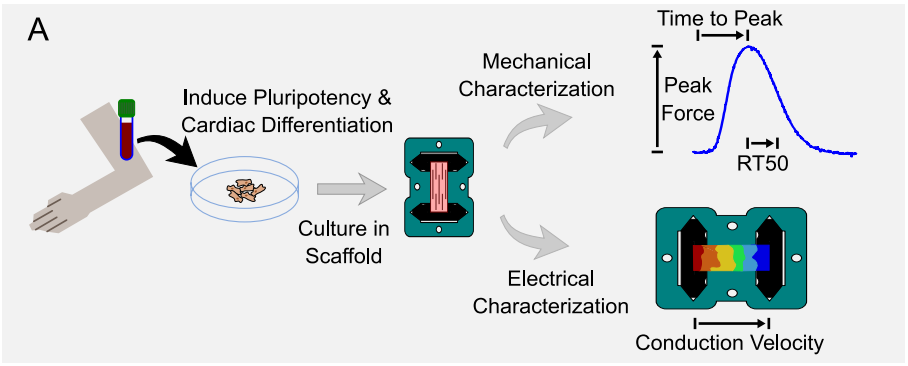

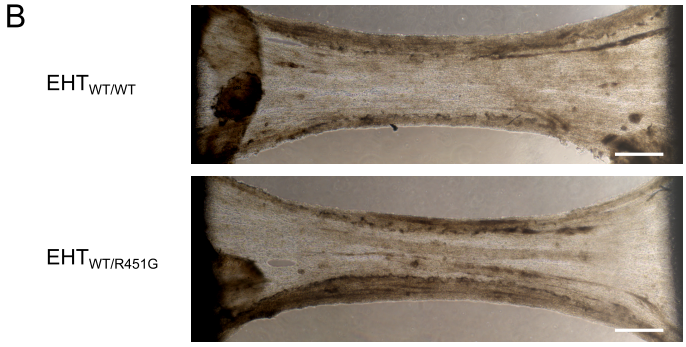

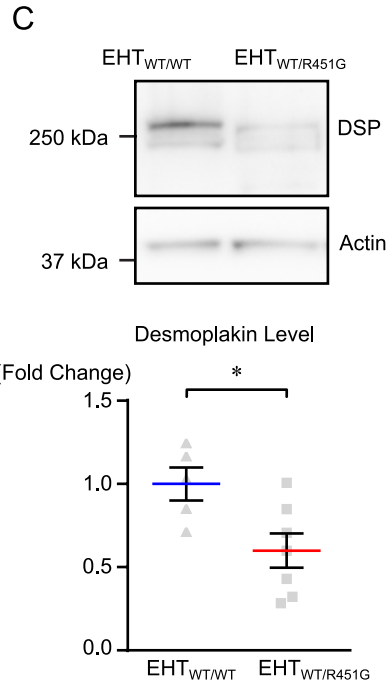

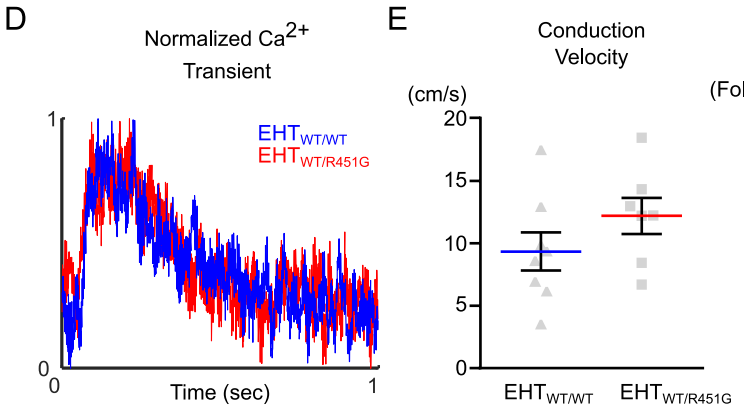

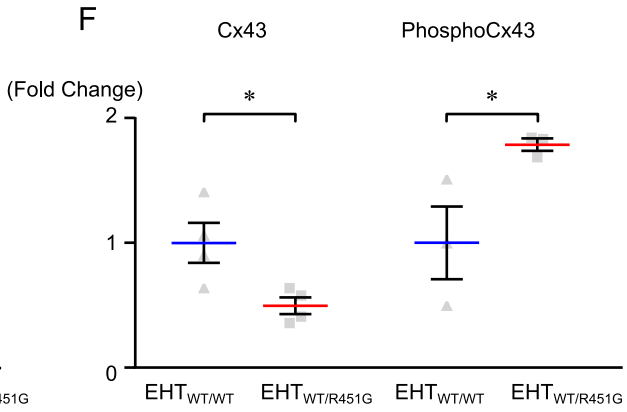

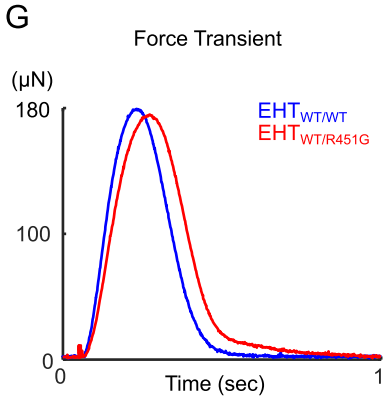

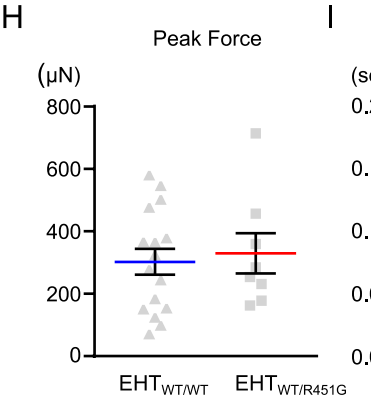

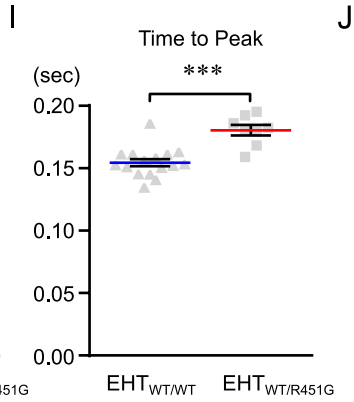

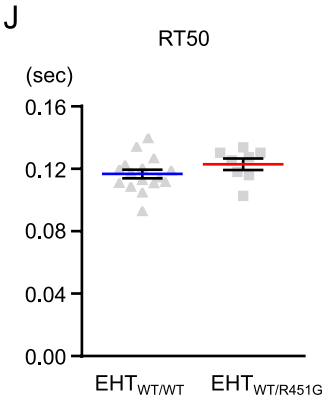

Figure caption on following page

Figure 3: Engineered Heart Tissues (EHTs) from patient-derived induced pluripotent stem cells (iPSCs) exhibit reduced levels of desmoplakin. (A) EHTs were created by differentiating cardiomyocytes from patient-derived iPSCs and seeding cells into decellularized porcine myocardial slices. Constructs were used to assess contractility and electrical conduction velocity. **(B)** EHTs were generated using cardiomyocytes differentiated from G(+)P(+) patient III-36 and G(-)P(-) sibling III-35, denoted EHTWT/R451G and EHTWT/WT respectively. Brightfield images of EHTs show similar matrix compaction and morphology between the two types. Bars represent 1 millimeter. **(C)** Representative immunoblot of desmoplakin (DSP) protein levels in EHTs shows substantial loss in the patient-derived tissue, which was statistically significant when quantified across several samples (**P < 0.01 for 2-tailed unpaired t-test; n= 5 WT and n=7 R451G). **(D)** Ca2+ transients collected from EHTWT/R451G and EHTWT/WT showed no differences between the two tissue types. (**E)** Measurements of longitudinal conduction velocity in EHTs showed no differences between EHTWT/R451G and EHTWT/WT (unpaired t-test; n= 7 and 8 respectively). **(F)** Protein levels of connexin-43 (Cx43) and phosphorylated (Ser368) Cx43 in EHTs normalized to sarcomeric actin reveals significantly reduced Cx43 and significantly elevated levels of phosphorylated Cx43 in EHTWT/R451G (*P < 0.05 for 2-tailed unpaired t-test, n= 3). **(G)** Representative force transients collected simultaneously with above Ca2+ transients reveal a delayed time to peak force in EHTWT/R451G. **(H)** Maximal force produced by EHTs. **(I)** Time from stimulus to maximal force. **(J)** Time elapsed from point of maximal force to 50% relaxation (RT50). ***P < 0.001 for 2-tailed unpaired t-test with Bonferroni correction (n= 16 EHTWT/WT and n = 8 EHTWT/R451G). Error bars represent SEM.

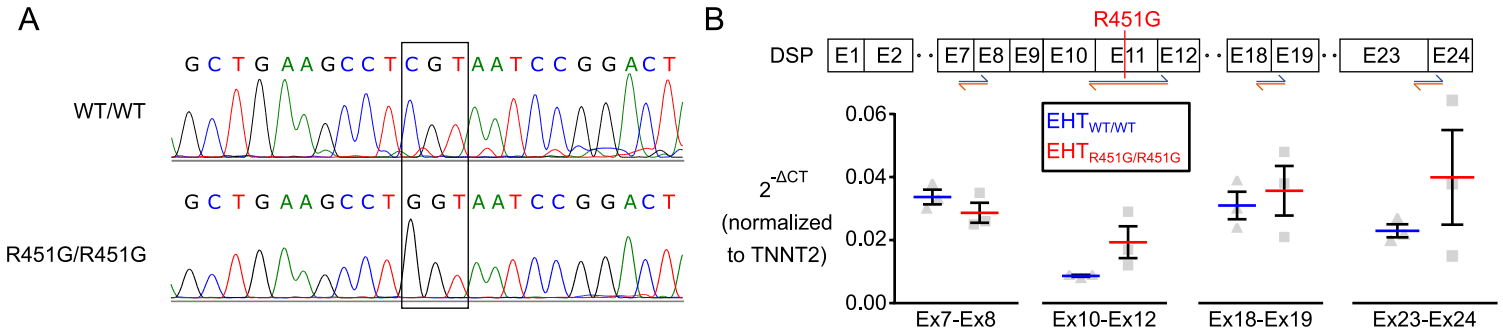

Figure 4: EHTs homozygous for R451G maintain normal levels of DSP mRNA (A) Genotyping of the control cell line (WT/WT) and the same cell line after CRISPR/Cas9 manipulation to introduce the DSP R451G mutation (ENST00000379802.8; c.1596CGT>GGT; Chr. 6:7568521, GRCh38.p12) at both alleles (R451G/R451G). **(B)** RT-qPCR was performed on engineered heart tissues formed from WT/WT and R451G/R451G cardiomyocytes in order to probe for DSP mRNA abundance. Several different primer pairs covering different exon junctions indicate that similar levels of DSP mRNA were expressed in both cell lines and that the introduction of c.1596CGT>GGT did not affect mRNA stability or result in alternative splicing (2-tailed unpaired t-test with Bonferroni correction; n=3). Blue and orange arrows represent regions targeted by forward and reverse primer pairs. Cycle thresholds were normalized to TNNT2 (cardiac troponin T).

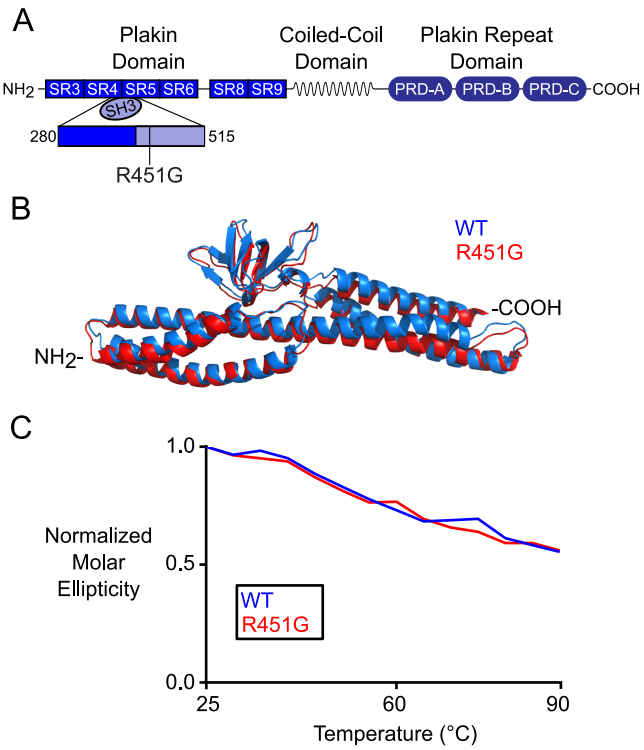

Figure 5: Glycine substitution at residue 451 results in no overt structural defects in desmoplakin. (A) Schematic of desmoplakin showing the location of the mutated residue (R451G). The mutation occurs near the NH2-terminus region, which is responsible for interacting with the armadillo proteins of the desmosome. **(B)** Overlaid structural models of wild type desmoplakin and desmoplakin with the R451G mutation after a 60 ns MD simulation. **(C)** Circular dichroism at 222 nm, normalized to 20oC for WT and R451G desmoplakin. As temperature was increased, both proteins showed similar degradation profiles.

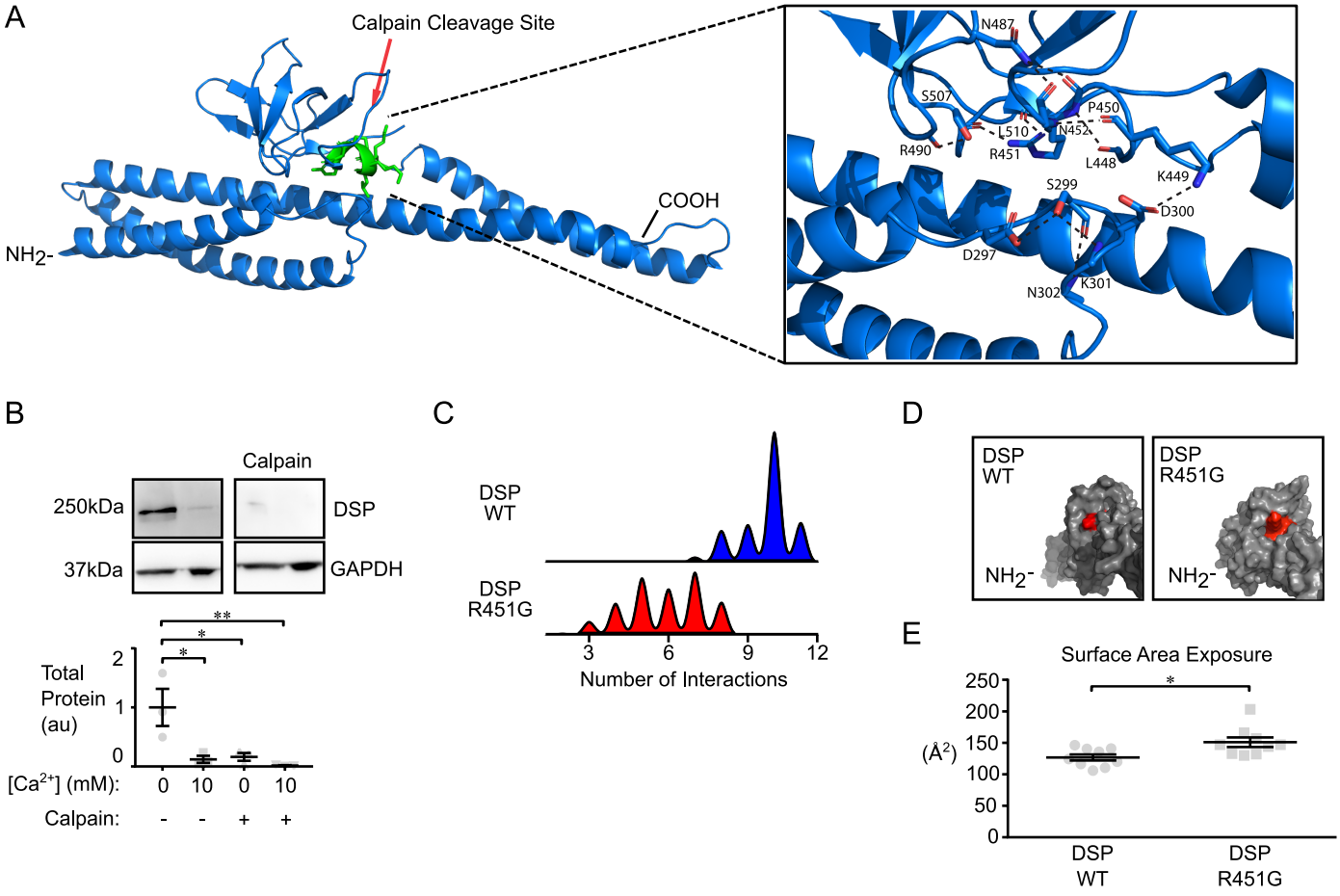

Figure 6: Increased exposure of a calpain target site on desmoplakin due to a glycine substitution at residue 451. **(A)** Ribbon model of desmoplakin showing location of affected calpain site (resides 447-451). Inset shows intramolecular interactions surrounding putative calpain site. **(B)** Immunoblots of lysates from a donor control heart (OSU 294050) for changes in desmoplakin levels following the addition of exogenous Ca2+ or calpain. Addition of 10 mM Ca2+ over endogenous levels results in significant degradation of desmoplakin (left). Addition of exogenous calpain further reduced levels of desmoplakin at both endogenous levels and increased levels of Ca2+ (*P < 0.05 , **P < 0.01 for 2-way ANOVA with Tukey's multiple comparisons test; n=3). **(C)** Histogram of the number of noncovalent interactions surrounding the calpain site, calculated from molecular dynamic simulations of wild type desmoplakin (blue) and R451G desmoplakin (red). R451G produced a clear reduction in the average number of non-covalent interactions surrounding the calpain site, possibly increasing solvent accessibility degradation rate. **(D)** Surface model of desmoplakin showing the exposure of the affected calpain site in WT desmoplakin (left) and R451G desmoplakin (right). Red represents exposed surface of calpain site residues. **(E)** Average exposed surface area of the calpain site over the length of the simulation (*P < 0.05, 2-tailed unpaired t-test; n=8) Error bars represent SEM.

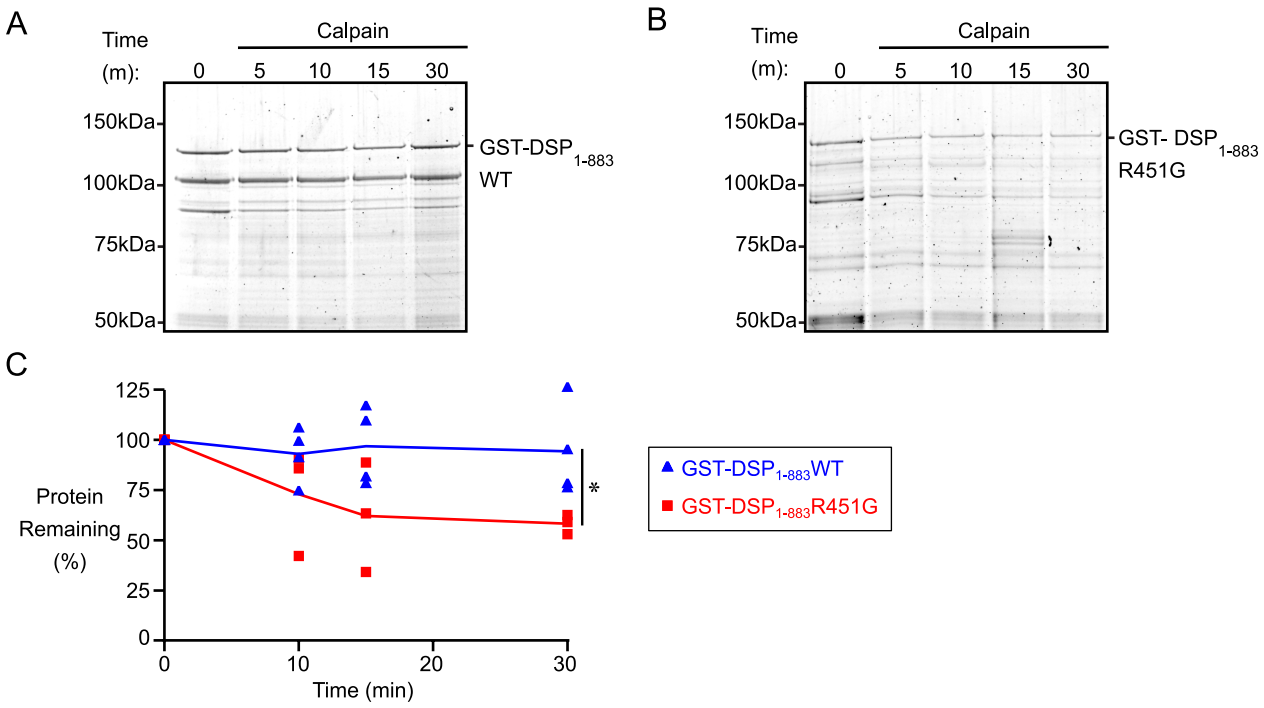

Figure 7: Decreased stability of recombinant desmoplakin NH2-terminus with R451G mutation. (A) A recombinant glutathione S-transferase tagged desmoplakin fragment consisting of the first 883 amino acids (GST-DSP1-883WT) was bacterially expressed and purified. After the fragment was incubated with calpain for 5, 10, 15, or 30 minute intervals, degradation products were separated via SDS-PAGE and visualized by staining with SyproRuby. Very little degradation was observed. **(B)** The same experiment was repeated with a fragment containing the R451G amino acid substitution (GST-DSP1-883R451G). This gel shows substantial decrease of the intact fragment over time as it is exposed to calpain. **(C)** Quantification of gel images across repeated experiments reveals a significant increase in calpain-mediated degradation of the mutant R451G recombinant DSP protein relative to WT (*$P < 0.05$ for 2-tailed unpaired t-test at 30-minute time point; GST-DSP1-883WT n=4; GST-DSP1-883R451G n=3). Error bars represent SEM.

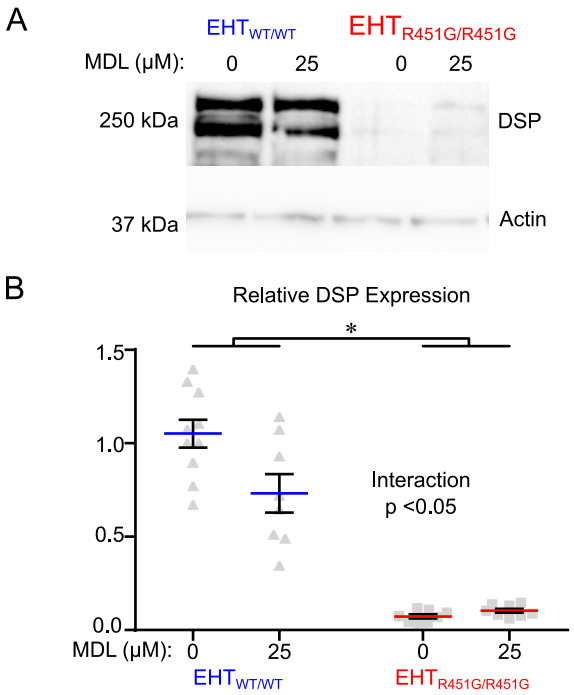

Figure 8: Calpain inhibition results in partial rescue of desmoplakin levels in homozygous DSP R451G EHTs. (A) Engineered heart tissues were incubated with 25μM of the calpain inhibitor MDL-28170(MDL) or a vehicle control (DMSO) for 72 hours and then probed for desmoplakin protein levels. Loading across gels was normalized by sarcomeric actin. (Gel images are representative of PGP1 MDL n = 10, PGP1 DMSO n=8, HO35 MDL n = 8, HO35 DMSO n = 8) **(B)** Quantification of immunoblot showing significant interaction between genotype and drug treatment. (*P<0.05 and significant interaction between genotype and drug treatment for 2-way ANOVA with Tukey's multiple comparisons test.) While desmoplakin levels in WT/WT EHTs were significantly decreased in samples exposed to MDL, this decrease was not observed in R451G/R451G EHTs.

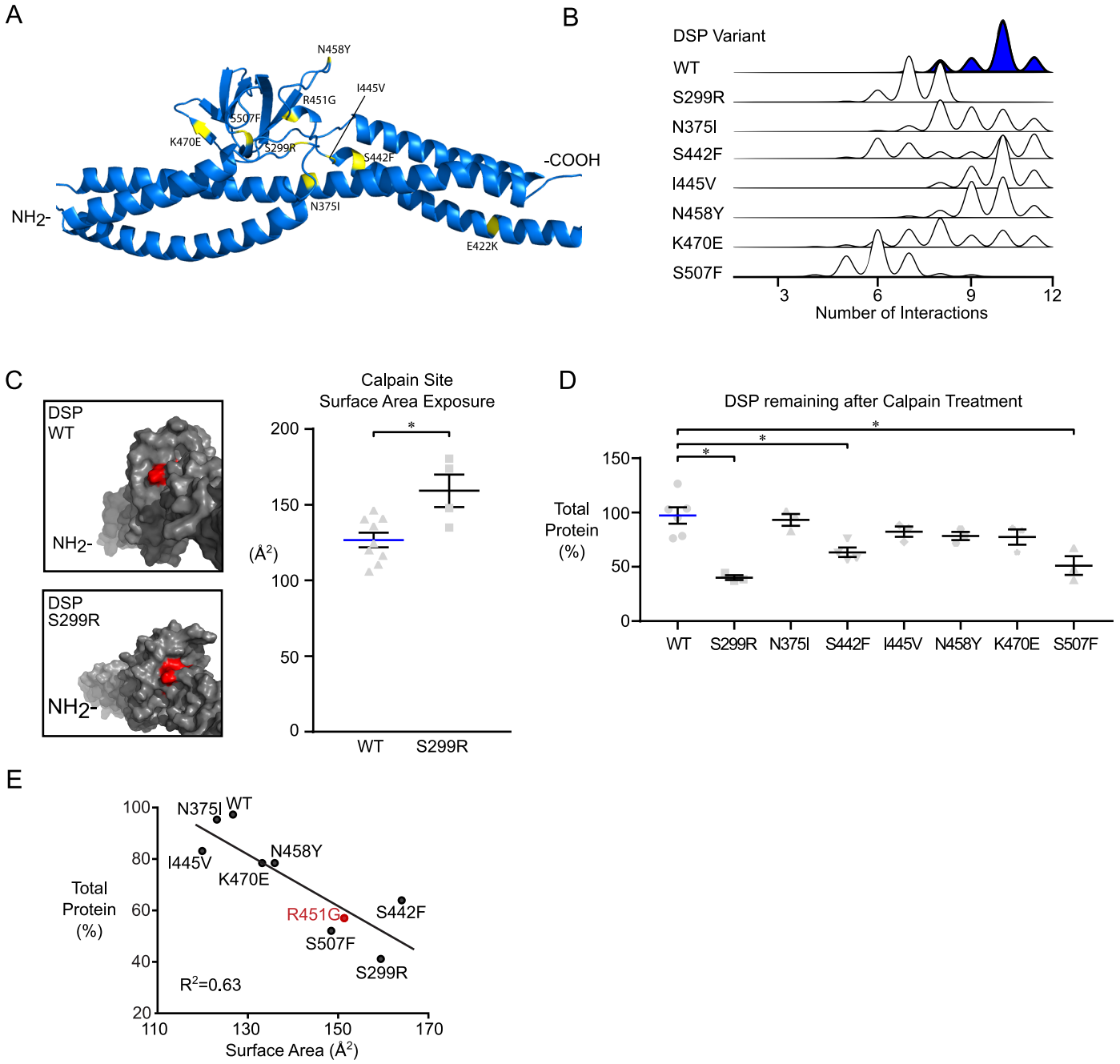

Figure 9: Increased calpain degradation is common to other ACM-linked mutations in DSP. (A) Model showing the location of 7 other ACM-linked desmoplakin mutations in relation to the R451G variant. Together, these mutations constitute a potential hotspot with shared molecular pathology. **(B)** Molecular dynamic simulations were run on these 7 additional ACM-linked mutations, and the number of intramolecular interactions around the calpain target site were calculated. Histograms showing the frequency of intramolecular interactions reveal a variety of mutation-associated changes, including reduced interactions for three mutants in particular (S299R, S442F, and S507F). **(C)** Models of desmoplakin showing the surface exposure of the affected calpain site (red) suggest that exposure in S299R desmoplakin is greater than for the WT structure. This predicted increase was statistically significant when examined across several repeat simulations (*P < 0.05, 2-tailed t-test, n=9 WT and n=4 S299R). **(D)** Each of the seven hotspot mutations was recombinantly expressed in DSP NH2-terminal fragments, purified, and incubated with calpain and Ca2+ for 30 minutes. Total protein remaining was determined for each mutation. S299R, S442F, and S507F each showed significant degradation relative to WT fragment over the same interval (*P < 0.05 for 1-way ANOVA with Tukey's multiple comparisons test; WT n=3; variants n=3). Error bars represent SEM. **(E)** In order to test the predictive ability of the molecular dynamic simulations, regression analysis was performed on predicted calpain site surface area exposure and percent desmoplakin remaining after calpain treatment for each variant and wild type. The two quantities were significantly correlated (R2 = 0.63, P < 0.05, linear regression analysis).

Table 1:

G(+)P(+) patients with available medical records (n)	15
Demographics and clinical information	
Age (years)	44.9±15.1
Sex (M/F) (n)	4/11
BMI (kg/m2)	25.8±6.8
SBP (mm Hg)	116.8±18.4
DBP (mm Hg)	72.6±8.1
HR (bpm)	72.4±6.8
Antiarrhythmic medication (n)	8
ICD implanted (n)	5
Ventricular involvement	
Biventricular ACM (n)	5
ALVC (n)	6
ARVC (n)	1
Left ventricular function	
LVEF>=55% (n)	4
LVEF 35-55% (n)	6
LVEF <=35% (n)	2
Fibrosis (LGE) on CMR (n)	4
Events and outcomes	
Sustained VT (n)	3
NSVT (n)	6
Syncope (n)	4
SCD episodes (n)	6
Age at SCD (years)	40.6±16.2

G(+)P(-) patients with available medical records (n)	6
Demographics and clinical information	
Age (years)	34.8±8.1
Sex (M/F) (n)	0/6
BMI (kg/m2)	24.6±3.0
SBP (mm Hg)	110.5±11.0
DBP (mm Hg)	68.3±7.6
HR (bpm)	77.2±7.1

Table 2:

Mutation	Surface Area Exposure ($Å^2$) ± SD
WT	127 ± 4.88
S299R	159 ± 10.7
N375I	123 ± 4.5
S442F	164 ± 7.3
I445V	120 ± 4
R451G	151 ± 7.6
N458Y	136 ± 7.5
E470K	133 ± 7.3
S507F	148 ± 8.6

References

1. Corrado D, Link MS, Calkins H. Arrhythmogenic Right Ventricular Cardiomyopathy. N Engl J Med. 2017;376(1):61–72.

2. Crossley GH, Poole JE, Rozner MA, Asirvatham SJ, Cheng A, Chung MK, et al. The Heart Rhythm Society (HRS)/American Society of Anesthesiologists (ASA). Hear Rhythm [Internet]. 2011;8(7):1114–52. Available from: http://dx.doi.org/10.1016/j.hrthm.2010.12.023

3. Corrado D, Basso C, Thiene G, McKenna WJ, Davies MJ, Fontaliran F, et al. Spectrum of Clinicopathologic Manifestations of Arrhythmogenic Right Ventricular Cardiomyopathy/Dysplasia: A Multicenter Study. J Am Coll Cardiol [Internet]. 1997 Nov 15 [cited 2019 Jan 30];30(6):1512–20. Available from: https://www.sciencedirect.com/science/article/pii/S073510979700332X?via%3Dihub

4. Sen-Chowdhry S, Syrris P, Prasad SK, Hughes SE, Merrifield R, Ward D, et al. Left-dominant arrhythmogenic cardiomyopathy: an under-recognized clinical entity. J Am Coll Cardiol. 2008 Dec;52(25):2175–87.

5. Srijita S-C, Petros S, Deirdre W, Angeliki A, Elias S, J. MW. Clinical and Genetic Characterization of Families With Arrhythmogenic Right Ventricular Dysplasia/Cardiomyopathy Provides Novel Insights Into Patterns of Disease Expression. Circulation [Internet]. 2007 Apr 3;115(13):1710–20. Available from: https://doi.org/10.1161/CIRCULATIONAHA.106.660241

6. Bhonsale A, Murray B, Tichnell C, James CA, Judge DP, Tandri H, et al. Impact of genotype on clinical course in arrhythmogenic right ventricular dysplasia/cardiomyopathy-associated mutation carriers. Eur Heart J [Internet]. 2015 Jan 23;36(14):847–55. Available from: https://dx.doi.org/10.1093/eurheartj/ehu509

7. López-Cuenca D, López-Ayala JM, González-Carrillo J, Sánchez Muñoz JJ, Oliva-Sandoval MJ,

Valdés M, et al. Desmoplakin truncations and arrhythmogenic left ventricular cardiomyopathy: characterizing a phenotype. EP Eur [Internet]. 2014 Jun 17;16(12):1838–46. Available from: https://dx.doi.org/10.1093/europace/euu128

8. Bauce B, Basso C, Rampazzo A, Beffagna G, Daliento L, Frigo G, et al. Clinical profile of four families with arrhythmogenic right ventricular cardiomyopathy caused by dominant desmoplakin mutations. Eur Heart J. 2005;26(16):1666–75.

9. Castelletti S, Vischer AS, Syrris P, Crotti L, Spazzolini C, Ghidoni A, et al. Desmoplakin missense and non-missense mutations in arrhythmogenic right ventricular cardiomyopathy: Genotype-phenotype correlation. Int J Cardiol. 2017 Dec;249:268–73.

10. Alcalde M, Campuzano O, Berne P, García-Pavía P, Doltra A, Arbelo E, et al. Stop-Gain Mutations in PKP2 Are Associated with a Later Age of Onset of Arrhythmogenic Right Ventricular Cardiomyopathy. Sovari AA, editor. PLoS One [Internet]. 2014 Jun 26 [cited 2019 Jan 31];9(6):e100560. Available from: https://dx.plos.org/10.1371/journal.pone.0100560

11. Hainque B, Simon F, Fressart V, Cosnay P, Scanu P, Extramiana F, et al. Desmosomal gene analysis in arrhythmogenic right ventricular dysplasia/cardiomyopathy: spectrum of mutations and clinical impact in practice. EP Eur [Internet]. 2010 Apr 16;12(6):861–8. Available from: https://dx.doi.org/10.1093/europace/euq104

12. Rasmussen TB, Hansen J, Nissen PH, Palmfeldt J, Dalager S, Jensen UB, et al. Protein expression studies of desmoplakin mutations in cardiomyopathy patients reveal different molecular disease mechanisms. Clin Genet [Internet]. 2013 Jul 1;84(1):20–30. Available from: https://doi.org/10.1111/cge.12056

13. Patel DM, Dubash AD, Kreitzer G, Green KJ. Disease mutations in desmoplakin inhibit Cx43 membrane targeting mediated by desmoplakin-EB1 interactions. J Cell Biol. 2014;206(6):779–97.

14. Eloff BC, Lerner DL, Yamada KA, Schuessler RB, Saffitz JE, Rosenbaum DS. High resolution optical mapping reveals conduction slowing in connexin43 deficient mice. Cardiovasc Res [Internet]. 2001;51(4):681–90. Available from: http://www.ncbi.nlm.nih.gov/pubmed/11530101

15. Smyth JW, Zhang S-S, Sanchez JM, Lamouille S, Vogan JM, Hesketh GG, et al. A 14-3-3 Mode-1 Binding Motif Initiates Gap Junction Internalization During Acute Cardiac Ischemia. Traffic [Internet]. 2014 Jun 1;15(6):684–99. Available from: https://doi.org/10.1111/tra.12169

16. Green KJ, Parry DA, Steinert PM, Virata ML, Wagner RM, Angst BD, et al. Structure of the human desmoplakins. Implications for function in the desmosomal plaque. J Biol Chem. 1990 Feb;265(5):2603–12.

17. Rampazzo A, Nava A, Malacrida S, Beffagna G, Bauce B, Rossi V, et al. Mutation in Human Desmoplakin Domain Binding to Plakoglobin Causes a Dominant Form of Arrhythmogenic Right Ventricular Cardiomyopathy. Am J Hum Genet [Internet]. 2002;71(5):1200–6. Available from: http://linkinghub.elsevier.com/retrieve/pii/S0002929707604145

18. Tan BY, Jain R, den Haan AD, Chen Y, Dalal D, Tandri H, et al. Shared desmosome gene findings in early and late onset arrhythmogenic right ventricular dysplasia/cardiomyopathy. J Cardiovasc Transl Res. 2010 Dec;3(6):663–73.

19. den Haan AD, Tan BY, Zikusoka MN, Llado LI, Jain R, Daly A, et al. Comprehensive desmosome mutation analysis in north americans with arrhythmogenic right ventricular dysplasia/cardiomyopathy. Circ Cardiovasc Genet. 2009 Oct;2(5):428–35.

20. Basso C, Czarnowska E, Della Barbera M, Bauce B, Beffagna G, Wlodarska EK, et al. Ultrastructural evidence of intercalated disc remodelling in arrhythmogenic right ventricular cardiomyopathy: an electron microscopy investigation on endomyocardial biopsies. Eur Hear J [Internet]. 2006;27. Available from: https://doi.org/10.1093/eurheartj/ehl095

21. Daday C, Kolšek K, Gräter F. The mechano-sensing role of the unique SH3 insertion in plakin domains revealed by Molecular Dynamics simulations. Sci Rep. 2017;7(1):1–10.

22. Kirchner F, Schuetz A, Boldt L-H, Martens K, Dittmar G, Haverkamp W, et al. Molecular Insights into Arrhythmogenic Right Ventricular Cardiomyopathy Caused by Plakophilin-2 Missense Mutations. Circ Cardiovasc Genet [Internet]. 2012;5(4):400–11. Available from: http://circgenetics.ahajournals.org/cgi/doi/10.1161/CIRCGENETICS.111.961854

23. Schrödinger, LLC. The {PyMOL} Molecular Graphics System, Version~1.8. 2015 Nov.

24. Wickham H. ggplot2: Elegant Graphics for Data Analysis [Internet]. Springer-Verlag New York; 2009. Available from: http://ggplot2.org

25. Choi H-J, Weis WI. Crystal structure of a rigid four-spectrin-repeat fragment of the human desmoplakin plakin domain. J Mol Biol. 2011 Jun;409(5):800–12.

26. Wilders R. Arrhythmogenic right ventricular cardiomyopathy: Considerations from in silico experiments. Front Physiol. 2012;3 MAY(May):1–11.

27. Blazeski A, Kostecki GM, Tung L. Engineered heart slices for electrophysiological and contractile studies. Biomaterials [Internet]. 2015;55:119–28. Available from: http://www.sciencedirect.com/science/article/pii/S014296121500304X

28. Dalal D, Tandri H, Judge DP, Amat N, Macedo R, Jain R, et al. Morphologic Variants of Familial Arrhythmogenic Right Ventricular Dysplasia/Cardiomyopathy. J Am Coll Cardiol [Internet]. 2009 Apr 14;53(15):1289 LP – 1299. Available from: http://www.onlinejacc.org/content/53/15/1289.abstract

29. Ertz-Berger BR, He H, Dowell C, Factor SM, Haim TE, Nunez S, et al. Changes in the chemical and dynamic properties of cardiac troponin T cause discrete cardiomyopathies in transgenic mice. Proc Natl Acad Sci [Internet]. 2005 Dec 13 [cited 2019 Feb 11];102(50):18219–24. Available

from: https://www.pnas.org/content/102/50/18219

30. Asimaki A, Tandri H, Huang H, Halushka MK, Gautam S, Basso C, et al. A new diagnostic test for arrhythmogenic right ventricular cardiomyopathy. N Engl J Med. 2009 Mar;360(11):1075–84.

31. Lyon RC, Mezzano V, Wright AT, Pfeiffer E, Chuang J, Banares K, et al. Connexin defects underlie arrhythmogenic right ventricular cardiomyopathy in a novel mouse model. Hum Mol Genet. 2014;23(5):1134–50.

32. Asimaki A, Kapoor S, Plovie E, Arndt AK, Adams E, Liu ZZ, et al. Identification of a new modulator of the intercalated disc in a zebrafish model of arrhythmogenic cardiomyopathy. Sci Transl Med. 2014;6(240):1–16.

33. Chelko SP, Asimaki A, Andersen P, Bedja D, Amat-Alarcon N, DeMazumder D, et al. Central role for GSK3β in the pathogenesis of arrhythmogenic cardiomyopathy. JCI insight [Internet]. 2016;1(5):1–20. Available from: http://www.ncbi.nlm.nih.gov/pubmed/27170944%5Cnhttp://www.pubmedcentral.nih.gov/articlerender.fcgi?artid=PMC4861310

34. Van Driest SL, Ommen SR, Tajik AJ, Gersh BJ, Ackerman MJ. Yield of Genetic Testing in Hypertrophic Cardiomyopathy. Mayo Clin Proc [Internet]. 2005;80(6):739–44. Available from: http://linkinghub.elsevier.com/retrieve/pii/S0025619611615279

35. Kapplinger JD, Landstrom AP, Salisbury BA, Callis TE, Pollevick GD, Tester DJ, et al. Distinguishing arrhythmogenic right ventricular cardiomyopathy/dysplasia-associated mutations from background genetic noise. J Am Coll Cardiol. 2011 Jun;57(23):2317–27.

36. Andreasen C, Nielsen JB, Refsgaard L, Holst AG, Christensen AH, Andreasen L, et al. New population-based exome data are questioning the pathogenicity of previously cardiomyopathy-associated genetic variants. Vol. 21, European Journal of Human Genetics. 2013. p. 918–28.

37. Guo A, Wang Y, Chen B, Wang Y, Yuan J, Zhang L, et al. E-C coupling structural protein junctophilin-2 encodes a stress-adaptive transcription regulator. Science (80-). 2018;362(6421):eaan3303.

38. Caspi O, Huber I, Gepstein A, Arbel G, Maizels L, Boulos M, et al. Modeling of arrhythmogenic right ventricular cardiomyopathy with human induced pluripotent stem cells. Circ Cardiovasc Genet. 2013;6(6):557–68.

39. Kim C, Wong J, Wen J, Wang S, Wang C, Spiering S, et al. Studying arrhythmogenic right ventricular dysplasia with patient-specific iPSCs. Nature [Internet]. 2013;494(7435):105–10. Available from: http://dx.doi.org/10.1038/nature11799

40. Ott J. Estimation of the recombination fraction in human pedigrees: efficient computation of the likelihood for human linkage studies. Am J Hum Genet. 1974;26:588–97.

41. Ackermann MA, Petrosino JM, Manring HR, Wright P, Shettigar V, Kilic A, et al. TGF-β1 affects cell-cell adhesion in the heart in an NCAM1-dependent mechanism. J Mol Cell Cardiol [Internet]. 2017;112:49–57. Available from: http://www.sciencedirect.com/science/article/pii/S0022282817303012

42. Hu L-YR, Ackermann MA, Hecker PA, Prosser BL, King B, O'Connell KA, et al. Deregulated Ca(2+) cycling underlies the development of arrhythmia and heart disease due to mutant obscurin. Sci Adv. 2017 Jun;3(6):e1603081.

43. Kopan R, Goate A, Dunn KW, Kamocka MM, Mcdonald JH. A practical guide to evaluating colocalization in biological microscopy. Genes Dev. 2011;46202(314):723–42.

44. Friedrich P, Tompa P, Farkas A. The calpain-system of Drosophila melanogaster: coming of age. Bioessays. 2004 Oct;26(10):1088–96.

45. Ackermann MA, King B, Lieberman NAP, Bobbili PJ, Rudloff M, Berndsen CE, et al. Novel

obscurins mediate cardiomyocyte adhesion and size via the PI3K/AKT/mTOR signaling pathway. J Mol Cell Cardiol. 2017 Oct;111:27–39.

46. Rudloff MW, Woosley AN, Wright NT. Biophysical characterization of naturally occurring titin M10 mutations. Protein Sci. 2015 Jun;24(6):946–55.

47. Godsel LM, Hsieh SN, Amargo E V, Bass AE, Pascoe-McGillicuddy LT, Huen AC, et al. Desmoplakin assembly dynamics in four dimensions: multiple phases differentially regulated by intermediate filaments and actin. J Cell Biol. 2005 Dec;171(6):1045–59.

48. Schafer DP, Jha S, Liu F, Akella T, McCullough LD, Rasband MN. Disruption of the axon initial segment cytoskeleton is a new mechanism for neuronal injury. J Neurosci. 2009 Oct;29(42):13242–54.

49. Smith SA, Hughes LD, Kline CF, Kempton AN, Dorn LE, Curran J, et al. Dysfunction of the beta2-spectrin-based pathway in human heart failure. Am J Physiol Heart Circ Physiol. 2016 Jun;310(11):H1583-91.

50. Pfaff M, Du X, Ginsberg MH. Calpain cleavage of integrin beta cytoplasmic domains. FEBS Lett. 1999 Oct;460(1):17–22.

51. Wang C-F, Huang Y-S. Calpain 2 activated through N-methyl-D-aspartic acid receptor signaling cleaves CPEB3 and abrogates CPEB3-repressed translation in neurons. Mol Cell Biol. 2012 Aug;32(16):3321–32.

52. Schwan J, Kwaczala AT, Ryan TJ, Bartulos O, Ren Y, Sewanan LR, et al. Anisotropic engineered heart tissue made from laser-cut decellularized myocardium. Sci Rep [Internet]. 2016;6:32068. Available from: http://www.nature.com/articles/srep32068